Microstructure Quantification of Oblique Angle Sputtered Porous a-Si Thin Films as a Basis for Structure-Property Relations of Solid Phase Microextraction Coatings

Behnam Moeini,<sup>1</sup> David T. Fullwood,<sup>2,\*</sup> Paul Minson,<sup>5</sup> Daniel Shollenberger,<sup>6</sup> David S. Bell,<sup>6</sup> Morris D. Argyle,<sup>3</sup> Richard Vanfleet,<sup>4</sup> and Matthew R. Linford<sup>1</sup>

<sup>1</sup>Departments of Chemistry and Biochemistry<sup>1</sup>, Mechanical Engineering<sup>2</sup>, Chemical Engineering,<sup>3</sup> and Physics and Astronomy,<sup>4</sup> Brigham Young University, Provo, UT 84602, USA <sup>5</sup>Electron Microscopy Facility, Brigham Young University, Provo, UT 84602, USA <sup>6</sup>Restek Corporation, 110 Benner Circle, Bellefonte, Pennsylvania 16823, United States

#### Abstract

Understanding processing-structure-property (PSP) linkages of solid-phase microextraction (SPME) coating materials is crucial for the rational design and advancement of these new materials. As SPME is a diffusion-based extraction technique, analyzing the morphology of its coating materials is important for optimizing its performance. In this study, we assess the morphological evolution of micro/mesoporous amorphous silicon (a-Si) thin films sputtered at an oblique angle onto silicon, which serve as models for support materials in SPME devices. The contrast of scanning transmission electron microscopy (STEM) images is enhanced via ZnO infiltration by atomic layer deposition (ALD). Various metrics, including physical descriptors and two-point statistics methods, are employed to follow the films' evolution. Analysis of the two-point correlation function reveals a simple ellipse/spherical local pore geometry in contrast to the longrange irregular arrangement of pores identified by a range of traditional and novel metrics. Additionally, analyzing the internal structure of the pores through homology metrics aligns well with the theoretical understanding of morphological evolution in oblique sputtered films. These analyses show that the "average ratio of principal moment of inertia", "Betti numbers", and "twopoint statistics" based metrics can capture valuable information during film growth.

The morphological analysis approach proposed in this study can be applied to analyze any nanoporous medium as a first step towards developing structure-property relationships that tie back to a given preparation method. Ultimately, a more extensive experimental and/or simulation-based study should confirm the correlations between these metrics and actual diffusion properties as the basis for process-structure-properties relations for improved design and optimization of these film.

## 1 Introduction

As a chemical extraction technique, SPME combines multiple operations that include sample collection, extraction, analyte enrichment, and analyte isolation from sample matrices. SPME has been used to extract analytes from gaseous, liquid, and solid matrices in many in vivo and in vitro studies. For example, SPME is used for pharmaceutical materials, water analysis, food analysis, and the environmental sciences [1–7]. SPME is an open bed, diffusion rate controlled extractive technology. In principle, SPME has two main steps: absorption/adsorption or partitioning of analytes between the sample matrix and the SPME extraction phase followed by desorption of the concentrated extract into an analytical instrument [8–10]. Many parameters can affect the kinetics of SPME. Some of these include fluid flow velocity, the diffusion coefficient of the analyte, and the radius or geometry of the analyte, e.g., cylindrical or spherical [11,12]. The main factor that affects SPME's extraction efficiency is mass transport in the absorption/adsorption and desorption processes [11]. Several strategies have been developed to address mass transport limitations **SPME** including changes in measurement conditions and/or geometry/morphology of its coatings [12]. One of these solutions is to develop nanoporous thin film coatings,[12,13] which have increased active surface areas [13–15]. Although "micro" (<2 nm)/"mesoporous" (<50 nm)[16] based SPME phases generally show improved performance, their morphology and internal structure can strongly affect the diffusion characteristics and related properties of a film [17–19]. For example, access to micro/mesopores is dominated by diffusive mass transport [20]. This paper seeks to contribute to the understanding of the optimization of such films by characterizing film morphology and internal pore networks to find metrics that capture diffusion-related properties of the film; the techniques presented here will provide a vital step towards understanding processing-structure-property (PSP) linkages for the future development of SPME.

The micro/mesoporous thin films investigated in this work were synthesized using oblique angle physical vapor deposition (OAPVD). OAPVD is a common method for reproducibly creating nanostructured thin films. OAPVD generally uses electron beam or thermal evaporation to transport target atoms to a surface at an oblique angle. In this study, OAPVD films were prepared by sputtering. The process parameters in OAPVD strongly affect the resultant pore morphology [21,22]. For example, shadowing in OAPVD creates nanosized porous columnar structures [23]. The termination of the pillars in OAPVD creates surface roughness, which increases with deposition angle [21,23]. In addition, the film morphology changes as the film thickness increases during a deposition. The OAPVD micro/mesoporous a-Si thin films in this work can be loosely categorized as two-phase (a-Si and void) random heterogeneous materials of the type studied by Torquato et al [24].

Microstructural characterization of random heterogeneous materials involves statistical tools developed for this purpose. Here, "microstructure" refers to the geometrical arrangement of the material at an appropriate length-scale, e.g., the micro or mesoscale, and "characterization" refers to a statistical representation of the material's morphology. An initial step towards the full characterization of the physical behavior of a film involves identifying suitable metrics to capture the pore morphology, where "suitable" indicates that a given metric relates to the structure-property linkages relevant to the film. There are two main approaches to the microstructural characterization of pore spaces. The first is averaging methods of local descriptors such as pore size, and the second is metrics that rely on microstructure statistical functions such as correlation functions, e.g., two-point correlations [25,26]. The simplest and most common metric for quantifying porosity is the volume fraction of the pores. However, no geometrical information is contained in this metric. Two-point statistics provide geometrical information about porous media, indicating the probability of the two phases being separated by any selected vector. However, long-range

connectivity is not captured by these statistics. Tortuosity is a long-range connectivity descriptor that relates to the shortest connected path from one part of a structure to another in one phase. It is thus related to the ease of diffusion in a material [27].

This work explores the application of a range of morphological metrics to the characterization of the pore structure of an a-Si micro/mesoporous support coating that has previously shown excellent extraction performance in SPME [28,29]. The goal is to identify how these metrics capture structure evolution with sputtering time and direction. Some of these metrics are: (i) the size (area and maximum diameter) distribution of the pores, (ii) the anisotropy/directionality of the pores, (iii) a metric that indicates tortuosity of the pore structure, (iv) Betti numbers (related to internal connectivity of the pore space), and (v) the two-point statistics of the pores – specifically, the two-point autocorrelation functions. These metrics are applied to 2D sections of multiple oblique-angle films sputtered/deposited for different times. These analyses were performed on scanning transmission electron microscopy (STEM) images. Initially, the metrics were applied to the x-y plane of a-Si/void films that were deposited by OAPVD sputtering of silicon for 5 to 60 min. The metrics were also applied to a cross-section (the x-z plane) of a thicker film, which showed that sputtering time affects film structure in the z direction. Prior to image processing of the thicker film its contrast was improved by ZnO infiltration into the pores using thermal atomic layer deposition (ALD) of dimethylzinc (DMZ) and water [30]. The methodology showcased in this work should be important both for the future development of SPME and any type of functional nanoporous medium.

### 2 Experimental

#### 2.1 Materials

A silicon target (purity 99.999%, 3" diameter x 0.125" thick, Plasmaterials, Inc. Livermore, CA) was used as the silicon source for the sputtering. Silicon wafers (Si(100), University Wafer Inc., South Boston, MA) were used as substrates for depositions of thick a-Si films. The ALD

precursor, DMZ, was purchased from Strem Chemicals (99.999%, Newburyport, MA, USA). The water used in the ALD process was HPLC grade. Thin (15-25 nm) carbon films on 200 mesh copper TEM grids were purchased from Ted Pella Inc., Redding, CA, and were used as substrates for sputtering thin a-Si films.

### 2.2 Instrumentation

PVD and ALD were performed with PVD-75, and ALD-150LX<sup>TM</sup> systems from Kurt J. Lesker Inc. (Kurt J. Lesker (Jefferson Hills, PA)). Silicon substrates were cleaned with a Basic Plasma Cleaner (115 V) from Harrick Plasma (Ithaca, NY). Helios NanoLab 600 DualBeam (FIB/SEM), and VeriosTM (ThermoFisher Scientific, Waltham, MA) microscopes were used for imaging and TEM sample preparation. A gallium focused ion beam (FIB) was used to make cross sections for SEM and TEM imaging. Line scan EDS for elemental analysis was performed to verify the presence of zinc in an infiltrated thick a-Si film.

## 2.3 Preparation of a-Si porous, thin films

a-Si was sputtered at an oblique angle onto silicon wafers and carbon/copper TEM mesh grids. The substrates were placed above the silicon target with their surfaces parallel to the flux of sputtered material. No heating or rotation was applied to the substrates. The throw distance, i.e., the shortest distance between the target and the substrate, was 20 cm in all depositions. DC sputtering was employed at 200 W power. The process gas was Ar at 5 mTorr. To study the effect of sputtering time on the film's evolution/morphology, twelve films were prepared by sputtering silicon onto carbon/copper TEM mesh grids for 5 to 60 min in 5 min increments.

### 2.4 ZnO infiltration

ZnO infiltration was performed by atomic layer deposition of ZnO inside the pores of sputtered a-Si films using dimethylzinc (DMZ) as the source of zinc, and water as the source of oxygen. Prior to deposition, the substrate was washed with methanol and plasma cleaned for one

minute. ALD was performed by applying 150 DMZ/water cycles with 21.0 ms, 10.0 s, 15.5 ms, and 10.0 s as the DMZ dose time,  $N_2(g)$  purge time, water dose time, and  $N_2(g)$  purge time, respectively. The temperature of the DMZ precursor and the sample/substrate were 110 °C, and 200 °C, respectively.

## 2.5 SEM and S/TEM imaging

Planar view and cross-sectional SEM imaging were performed using Verios and Helios microscopes (see details above). All the imaging was taken in an immersion mode using a throughthe-lens detector. SEM cross-section samples were prepared using the gallium focused ion beam after coating the full sample surface with conductive Au/Pd (20 nm) and the region of interest (ROI) with platinum (1 µm). The cross-section lamellae for the TEM and STEM imaging were prepared using a mechanical polishing sample preparation method. The STEM imaging of the ZnO infiltrated cross-section sample was performed on a film prepared using a gallium FIB milling liftout process. This film was also covered with a Au/Pd/Pt coating layer before the milling. The milling process was performed using a beam with voltage = 30 kV and current = 2.7 nA. After making a lamella, it was lifted out using an OmniProbe AutoProbe 200 system and placed on a copper TEM mesh grid by platinum welding. The welded lamella was then thinned to be ready for TEM imaging. TEM images were taken at 200 kV, a 100 µm C2 aperture, and a 20 µm objective aperture with a CCD detector. A 400 nm line was traced across the thick a-Si thin film in STEM mode, after which an EDS was performed to scan the elemental composition of the ZnO-infiltrated film. The sputter rate was calculated based on the thickness of the cross-sectional TEM image of the thick a-Si film. This film was  $600 \pm 10$  nm thick after 300 min of sputtering, which gives almost a 2 nm/min sputtering rate. Thus, the films obtained by sputtering for 5 – 60 min were ca. 10 - 120 nm thick.

## 2.6 Image processing of a-Si films created in 5-60 min depositions

Prior to morphological analysis, STEM images were processed in two steps. First, denoising was performed using a median filter with the Skimage image processing package in Python, ver. 3.8.8. Second, segmentation and binarization were carried out using a thresholding algorithm. Values for this algorithm were determined based on an EDS line profile across a-Si and void features in the corresponding STEM image. The threshold was adjusted to create a value for the edges of the features that were at the midpoint between the intensities for a-Si and void.

### 2.7 Image processing of thick a-Si films infiltrated with ZnO

The image processing of ZnO infiltrated films was the same as described in the previous section, with the only difference being the thresholding method. Due to the higher brightness of the zinc infiltrated regions compared to a-Si, mean adaptive thresholding was performed using the OpenCV image processing package in Python ver. 3.8.8. This procedure was applied to ZnO infiltrated images to find the edges between regions in the EDS line scans.

### 2.8 Morphological analysis

Random pore colorization and all the morphological analyses were performed using custom code written in the MATLAB programming environment (Version R2021b, Release No. 9.11.0.1809720, The MathWorks Inc., 1 Apple Hill Drive, Natick, MA).

### 2.8.1 Pore Area and porosity

These metrics were calculated based on the volume fraction of pores.

## 2.8.2 Anisotropy/directionality

Anisotropy can be quantified rather simply. For elliptical structures, the aspect ratio of the ellipse and the orientation of the major axis can indicate anisotropy and directionality. For the much more branched pore structures in the current films, a similar metric can be arrived at by considering the principal moments of inertia of connected pores. The ratio of these moments of inertia is

analogous to the aspect ratio, and the orientation of the principal moment of inertia will indicate directionality.

## 2.8.3 Relative surface area (RSA)

For the 2D sections of the films, the most relevant metric involves comparing the ratio of pore area to the square of the perimeter length. For a circle, this ratio is  $1/4\pi$ , which is the maximum value that any 2D shape can achieve. After normalizing the ratio for a given pore by that of a circle, we term this metric the "relative surface area (RSA)" of the pores.

### 2.8.4 Betti numbers

These metrics relate to the connectivity of materials' structure that comes from the field of homology. Homology in materials characterization refers to the concept of structural similarity or equivalence between different materials or components. Betti numbers are calculated based on homology theory [31]. They provide information about the number of "holes" or "cycles" of different dimensions in a given space. The zeroth Betti number (Betti\_0) represents the number of connected components in a space. The first Betti number (Betti\_1) counts the number of independent one-dimensional cycles, usually known as "loops". Betti numbers provide valuable information about the shape and connectivity of a space [32,33]. These metrics, were calculated using the CHomP software [34].

## 2.8.5 Two-point correlation function

In theory, this metric is based on the probability of landing both ends of a line with length r in a specific phase (pore space in this work). The two-point correlation function ( $f_2$ ) is defined in Equation 1,[35]

$$f_2(\vec{r}) = \frac{1}{vol(\Omega)} \int_{\Omega}^0 m^f(x) m^f(x + \vec{r}) dx \tag{1}$$

where  $\Omega$  is the total volume/area,  $m^f$  is the microstructure function, x is a point (pixel), and r is a length (pixel) that  $f_2$  applies on the volume. This function can be calculated by fast Fourier transform (FFT) on all the points (x) and all vectors  $\vec{r}$  very rapidly. If the average of  $f_2(\vec{r})$  is taken over all directions, i.e., for constant  $|\vec{r}|$ , then the resultant 1D statistics,  $f_2(r)$ , are termed the non-directional two-point statistics. The normalized two-point correlation function is obtained by dividing the non-directional statistics by their asymptotic value (Eq. 2), and is useful for extracting metrics; for example, this function has been used to show the clustering level of some aluminum composite materials [36].

$$f_2^*(r) = \frac{f_2(r)}{vf_2} \tag{2}$$

Two previously defined metrics [35] can be extracted from the normalized two-point statistics plots. The first metric is  $L_{\infty}$ , which is defined as the value of r when  $f_2^*$  is first within 2% of the asymptotic value (infinity value). In other words, the r value when  $f_2^* = 1.02$  is a measure of the width of the initial peak.

#### 3 Results and Discussion

3.1 Qualitative characterization of thick, porous, a-Si thin film using SEM and S/TEM imaging

Figure 1a shows that the sputtered films have cauliflower structures with multiple concentric, nearly spherical growth fronts with various size distributions/clustering levels. In general, the silicon clusters are separated, e.g., in the blue elliptical region, but in some areas they are connected, e.g., in the 76 nm x 247 nm region identified. Thus, silicon structures cluster mostly in elliptical shapes/patterns at this surface, separated by pores that fill the remaining area. The HRSEM cross-sectional view of this film in Figure 1b shows tilted, angled columnar structures in the sputtered silicon. Although HRSEM can distinguish the pillars, especially at the top of the film

where they are wider and better separated, it does not reveal a clear picture of the deeper structures, i.e., pore morphology, pore size, and spacing between the pillars. The deeper view of these films, shown in Figure 1c and d, was obtained from cross-sectional TEM and STEM images.

The shadowing effects in oblique-angle depositions often lead to ordered nanostructured films with controlled morphology and surface roughness, including pillars with nanometer-sized gaps, widths, and heights and tilted columnar structures [21,23]. The columnar features in Figure 1c are tilted  $22.7 \pm 0.4^{\circ}$  from the surface normal. Long, vertical, narrow pores between silicon pillars can potentially help analytes diffuse to the bottom of the film. They may also facilitate lateral diffusion in the film, which may increase extraction capacity. The TEM and STEM cross-sections in Figure 1c and d show an increased spacing between columns (pore size) as the columns approach the film surface. However, obtaining a clear picture of pore morphology at the bottom of the film is harder due to the decreased spacing between the columnar structures.

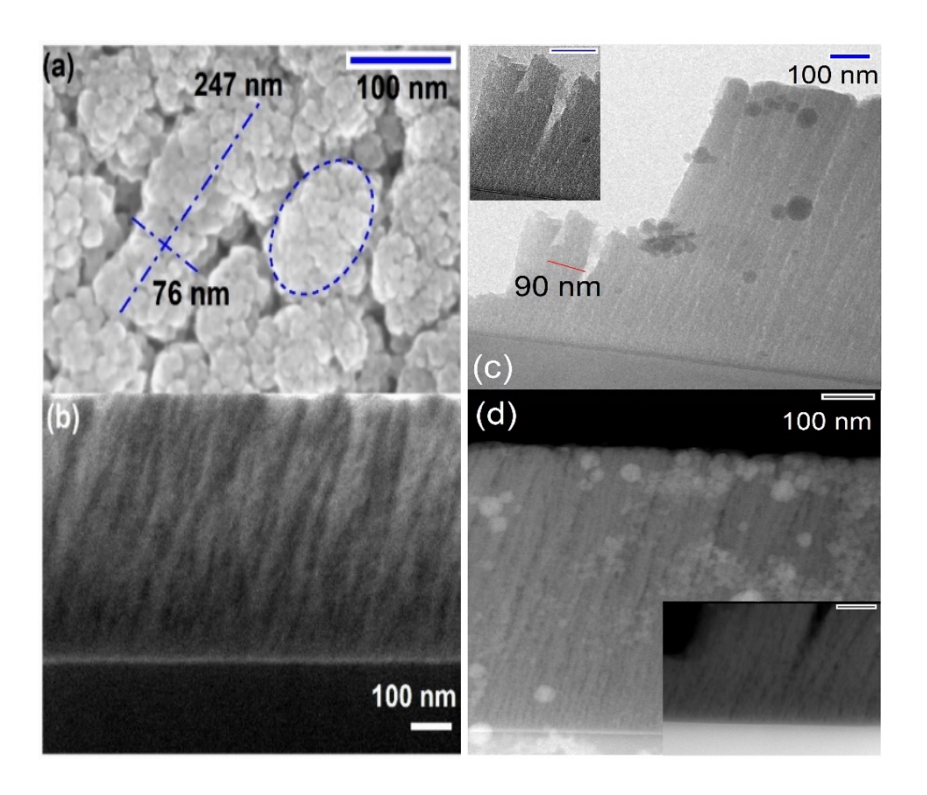


Figure 1. (a) Top-view (b), (c), and (d) cross-sectional HRSEM, TEM, and STEM images of a thick, sputtered a-Si film on silicon, respectively.

## 3.2 Quantitative microstructural characterization of pores in a-Si porous, thin films

Although the above S/TEM cross-sectional characterization of the sputtered a-Si thick film reveal useful information about the film's morphology and evolution, this information is mostly qualitative. Quantitative analysis of the morphology of the different phases in these films is required if future correlations between process parameters and material properties are to be extracted. To this end, twelve sputtered films with deposition times of 5 to 60 min were prepared (see Section 2.3). To increase the morphological information that can be obtained from these films, STEM imaging was used. It provides higher lateral resolution than parallel TEM imaging and information about film thickness and density, where its signal intensity is approximately proportional to the square of the atomic number ( $Z^2$ ) of the atom probed and the thickness of the specimen [37,38].

# 3.2.1 Analyzing of an initial film growth, i.e., 5-60 min a-Si porous, thin films

An initial, morphological evaluation of the thin sputtered films was performed using TEM imaging of a "5 min" film. These images (see Figure 2) show that the sputtered a-Si films are comprised of an a-Si matrix that is interrupted by a complex labyrinth of pores. Higher magnification of this structure (see Figure 2b) shows that these pores can be both very narrow, e.g., ca. 1.3 nm, and that they can also be connected together to form longer structures/pores. This complex pore network can affect the diffusion/mass transfer properties of these micro/mesoporous films. Therefore, a quantitative morphological analysis of these films could be very helpful in elucidating the structure-property linkages of this material for their future application in SPME.

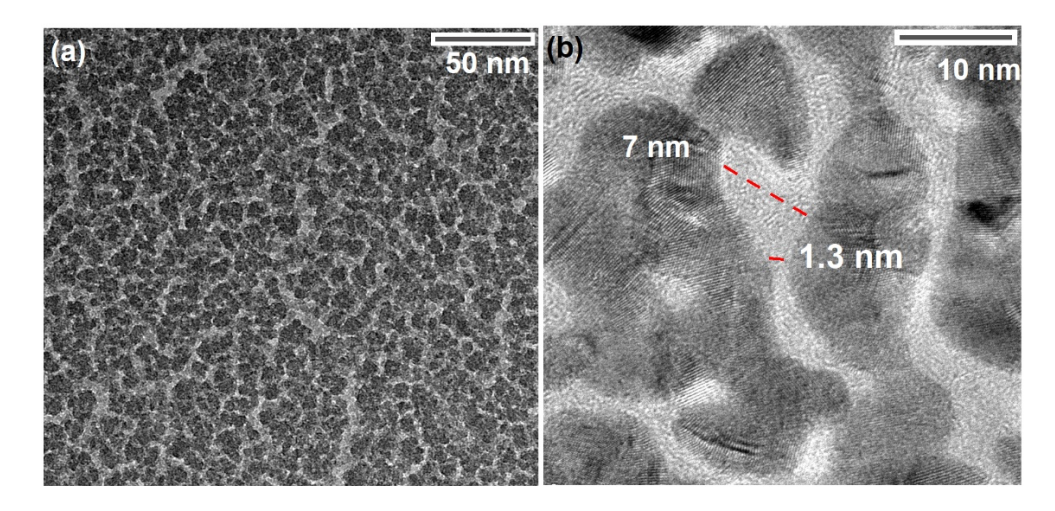


Figure 2. TEM images of (a) a 5 min sputtered a-Si film and (b) a higher magnification of the same film. Pores are brighter than silicon structures.

A quantitative, morphological analysis was performed on the images in Figure 3. Prior to this analysis, all the images were preprocessed as described in Section 2.6. In an additional step, pores with areas below 25 pixel<sup>2</sup> (~0.58 nm<sup>2</sup>) were eliminated as noise. Individual, connected regions of pores were then identified and labeled (see Figure 4), where each individual pore in a 2D structure is colored with a random color. Visual observation indicates a relatively homogeneous structure over the 200x200 nm regions, and that the feature size is significantly smaller than the window size; i.e. indicating that the regions being inspected are both representative, and of an appropriate size. However, to confirm this assumption, three areas of the same size were inspected for the coarsest structure (the 60 minute sample), and metrics of interest (discussed below) were compared for each. The standard deviation of key metrics (such as porosity, average pore size, diameter of peak of the two point statistics) were all around 3% of the mean value, indicating a high level of similarity in the statistics across the different regions.

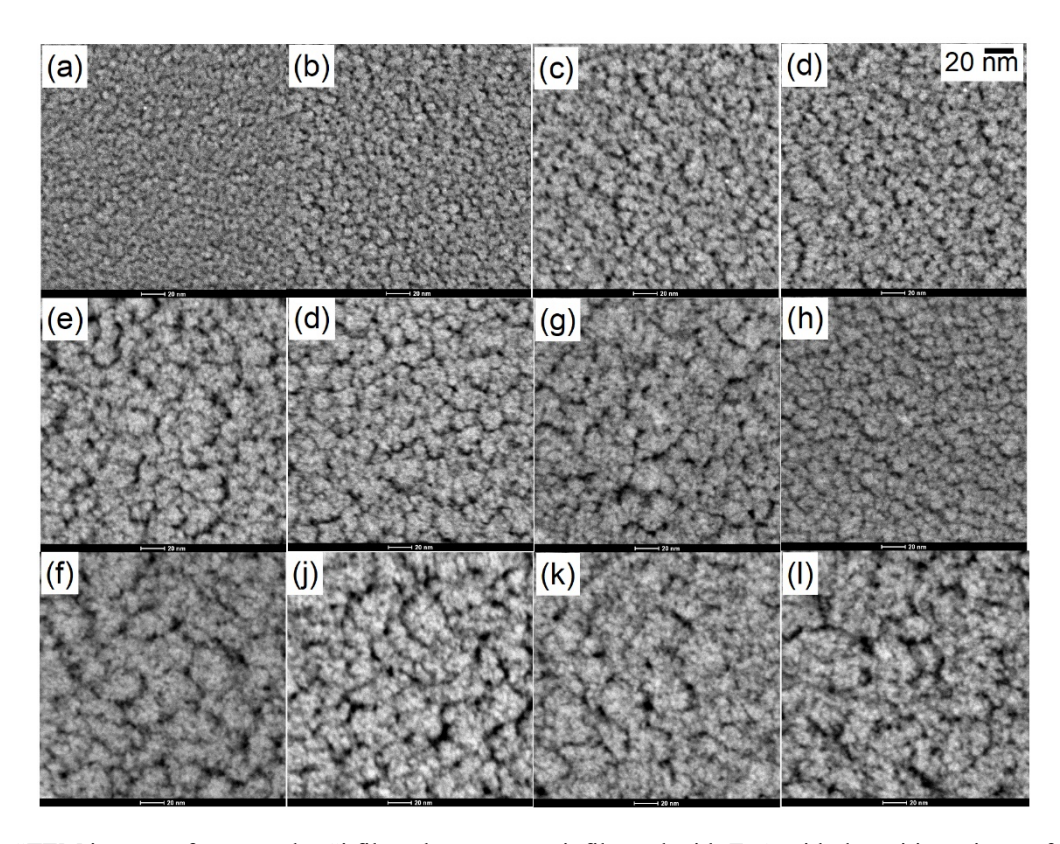


Figure 3. STEM images of sputtered a-Si films that were not infiltrated with ZnO with depositions times of (a) 5, (b) 10, (c) 15, (d) 20, (e) 25, (f) 30, (g) 35, (h) 40, (i) 45, (j) 50, (k) 55, and (l) 60 min.

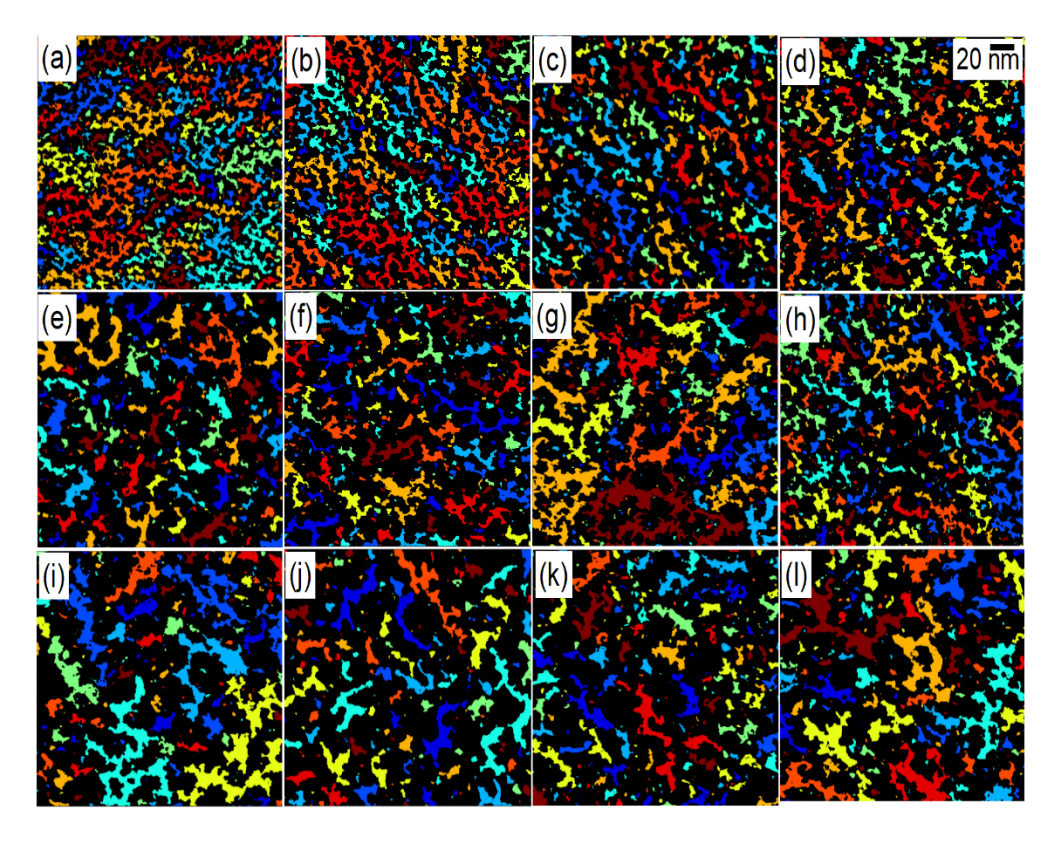


Figure 4. Processed STEM images of sputtered a-Si films (from Figure 3) with depositions times of (a) 5, (b) 10, (c) 15, (d) 20, (e) 25, (f) 30, (g) 35, (h) 40, (i) 45, (j) 50, (k) 55, and (l) 60 min, which show the connectivity of the pores as random colors.

### 3.2.1.1 Pore area and porosity

The processed images in Figure 4 reveal a high degree of connectivity and a complex branched pore structure. The average pore area in Figure 5a may show an increasing trend with sputtering time. Larger pore areas potentially can allow easier transport of analytes through the pores by increasing the diffusion flux. However, the overall volume fraction of pores (porosity) shows a slight decreasing trend with sputtering time, with a typical value of 30% porosity for these films (see Figure 5b).

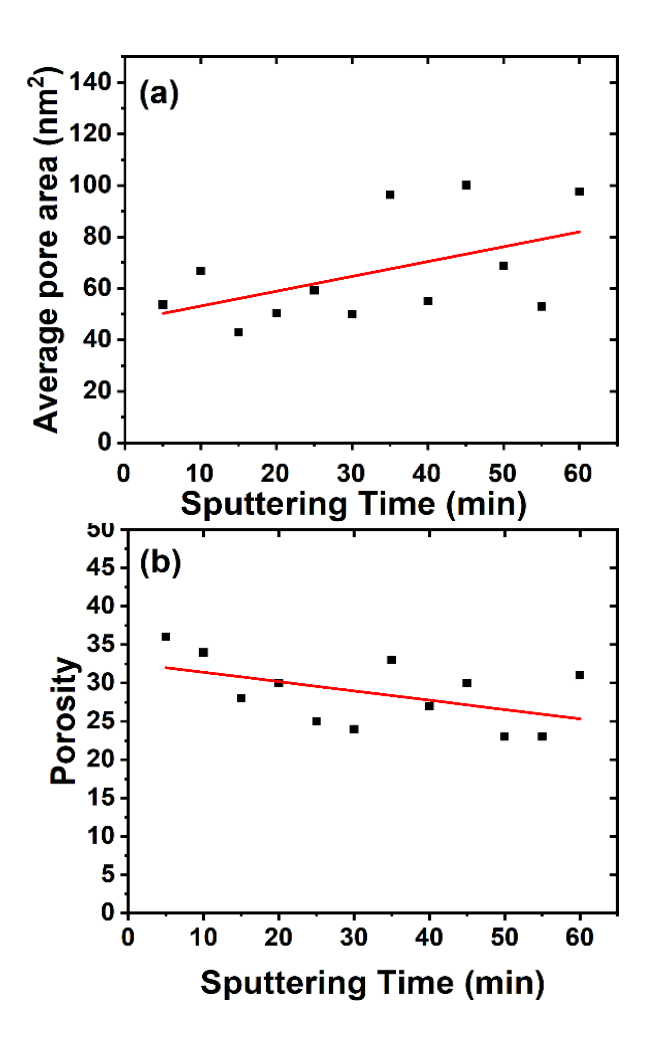


Figure 5. (a) Average pore area and (b) porosity of the 5-60 min sputtered a-Si thin films.

## 3.2.1.2 Anisotropy/directionality

Similar to the pore size, anisotropy/directionality of the pores might lead to biased diffusion behavior through the films. Figure 6 suggests that, at the beginning of the sputtering (5 - 15 min), the ratio of principal moment of inertia increases and then returns to an almost constant value. This indicates that even though the pore size is growing, the shape (at least, as quantified by the aspect ratio) remains relatively constant.

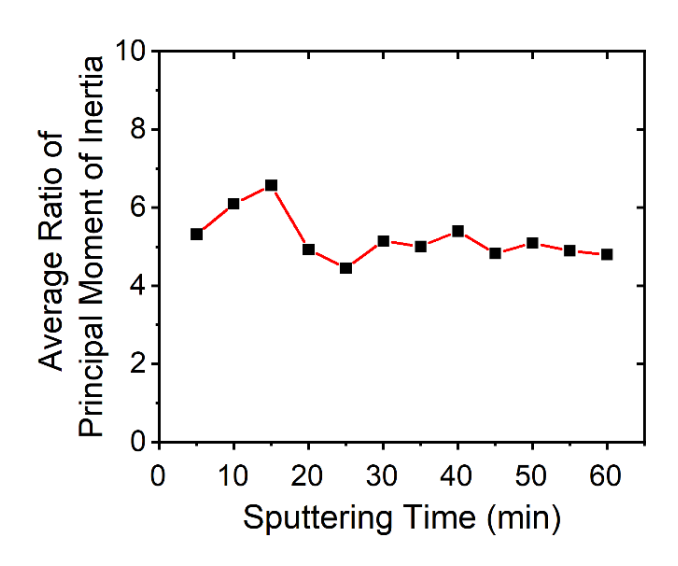


Figure 6. Average ratio of principal moment of inertia of the connected pores for the 5 – 60 min sputtered a-Si films.

## 3.2.1.3 Tortuosity

Porous media are often highly chaotic, resulting in paths for fluid flow and/or analytes that are significantly longer/different ( $L_p$ ) in length than a straight line ( $L_0$ ) in Figure 7 between the origin and the destination. A common definition for tortuosity is the ratio of average length that flow passes through the porous medium divided by the straight-line length across the film ( $L_p/L_0$ ) [39]. However, there are several definitions for tortuosity in the literature [40,41]. A metric that indicates tortuosity of the pore structures in our films is related to the surface area/branched nature of the pores – the relative surface area, RSA (see Section 2.8.3) - particularly for the larger pores that dominate the connectivity of the pore network; see Figure 7a. A larger value of RSA will indicate lower tortuosity and hence higher diffusivity because an effective diffusivity and  $\tau$  is the tortuosity, often with values around 2 to 3, which reduces the straight-line diffusion rate by that same factor.

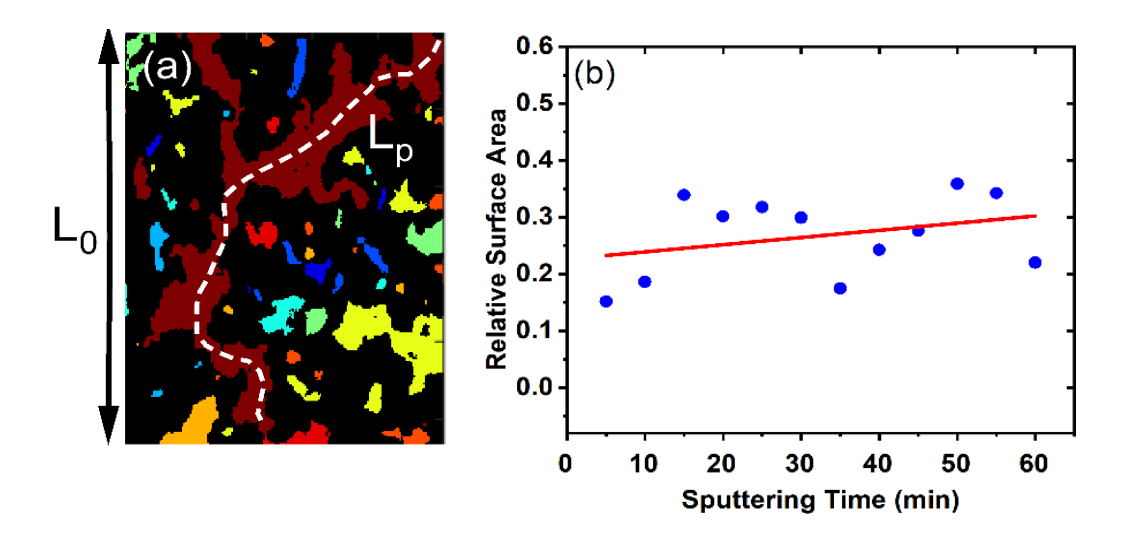


Figure 7. (a) The original concept of tortuosity is shown in the pore structure of the 60 min a-Si film. The double arrow  $(L_0)$  is the straight-line length from the bottom to the top of the image, while the dashed line  $(L_p)$  is an arbitrary actual length that an analyte needs to traverse to reach to the bottom of the image. (b) Relative surface area (RSA) of the pores for the 5-60 min a-Si films. While the relative surface area appears to be increasing, there is significant scatter about the red fit line.

As shown in Figure 7b, RSA values of the films show a slight increase with sputtering time. This observation confirms the conclusion drawn from the aspect ratio analysis, i.e., that the shape of the pores tends to remain relatively constant even as their size grows. The fact that the RSA trends slightly upward shows that the morphology of thicker films facilitates an analyte's diffusion through the film. This characteristic can be very important for deposition of much thicker films, (thicker films are desirable for SPME applications due to their higher surface areas and subsequent extraction capacities).

#### 3.2.1.4 Betti numbers

The pores in the 2D sections of the current films can be divided into disconnected components, the value of Betti\_0 indicates the number of disconnected pores, and the Betti\_1 parameter indicates the number of a-Si islands within the pores. Betti\_1 also relates to tortuosity, or the ease of finding a directly connected path across the film that lies entirely within pores. Hence the Betti\_1 parameter will also be quantified.

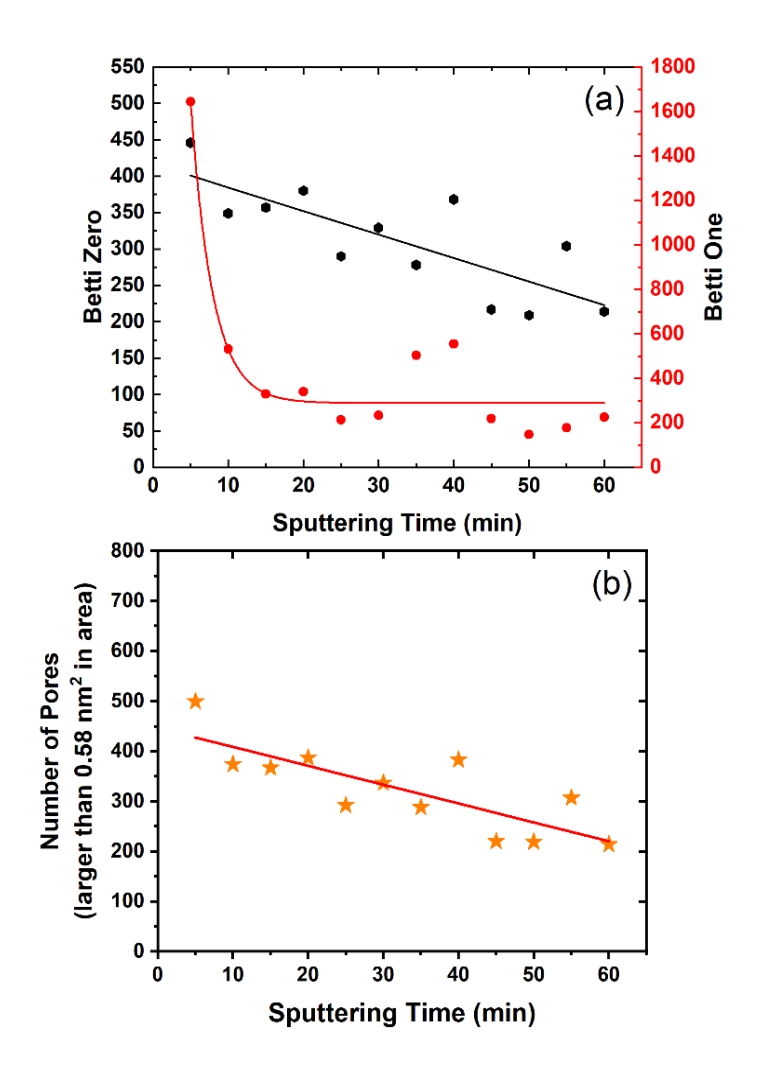


Figure 8. (a) Homology metrics, Betti $_0$  and Betti $_1$ , and (b) the number of pores larger than 5 by 5 pixels<sup>2</sup> or 0.58 nm<sup>2</sup> for the 5 – 60 min a-Si films.

As is shown in Figure 8a, Betti\_0 linearly decreases (albeit with a fair amount of scatter) with increasing sputtering time. The exponential decay of the Betti\_1 value in Figure 8a shows that the a-Si features grow around many nucleation points during the initial 15 minutes of sputtering, but that after, the columnar structures grow more stably and prohibit new island formation in the pore areas. The total number of pores with increasing sputtering times shown in Figure 8b displays the same decreasing trend as Betti\_0, such that the total number of pores decreases. This indicates that, in general, the connectedness of the pores in the pore space increases with increasing sputtering time. Lower Betti\_0 values, and associated larger/longer pores, suggest a potentially higher diffusion rate for the thicker films. However, lower numbers of a-Si islands in the pore areas

could result in high mass transfer rates. For example, tortuosity might decrease by lowering the Betti 1 value due to the small number of paths.

## 3.2.1.5 Two-point statistics

The two-point autocorrelation function is a widely used tool for characterizing the spatial structure of random fields like random heterogeneous films. The two-point statistics of the pores – specifically, the two-point autocorrelation functions – provide insights into the local connectivity of the pores. The standard two-point statistics do not contain information regarding long-range connectivity, but they generally indicate the morphology of locally connected regions. The peak in the center of the autocorrelation function indicates the shape of the region within the line-of-sight (while remaining within the pore phase) of a typical point within a pore. It can be thought of as indicating the typical shape (sphere/ellipse/other shape) that can be placed within a local pore region while remaining entirely within the pore. Hence, the aspect ratio of the central peak gives some indication of local anisotropy of the pores, while the ratio of principal moments of inertia relates to global anisotropy. Furthermore, the shape of the non-directional two-point statistics has been demonstrated to relate to clustering within a two-phase structure, which also affects diffusion [42].

Figure 9 shows an overlay of non-directional two-point correlation functions for the 5-60 min films. A typical  $f_2$  plot starts with a sharp drop as the probing vector (r) increases in length, i.e., as the distance from a random point in a pore increases, the probability of finding a-Si at the given radius increases. Figure 10 shows that, in general,  $f_2^*$  reveals three different patterns for the 5-20, 25-40, and 45-60 min films. Looking at these profiles shows that the first group reaches the asymptote value at lower values of r than the next two groups, presumably because of the smaller pore sizes. In the second group, i.e., 25-40 min films, more oscillation is observed as is shown in the other metrics as well. For example, 40 min films show much higher variation in

reaching the asymptote value than other films in this group. This reflects similar behavior to previously mentioned metrics, such as Betti numbers in Figure 8a, for this film.

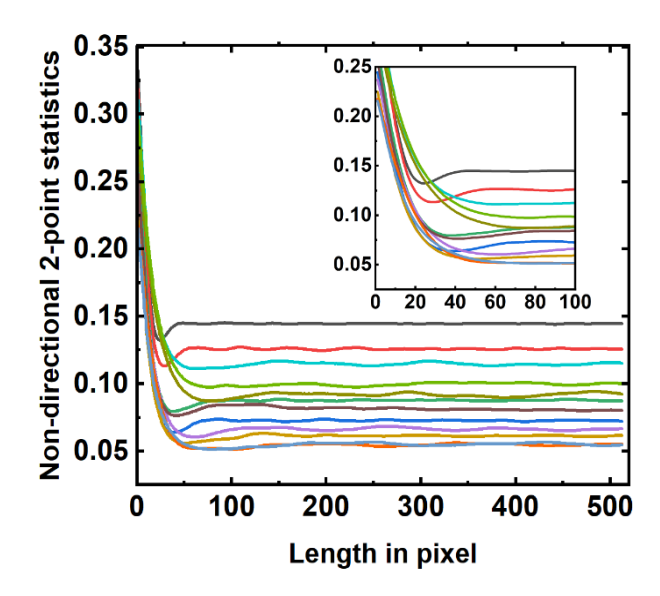


Figure 9. Overlay of non-directional two-point statistics of 5-60 min a-Si films through the length of r (512 pixels). The lines in the inset from high to low values at 100 pixels are for 5, 10, 35, 60, 45, 20, 40, 15, 25, 30, 55, and 15 min films.

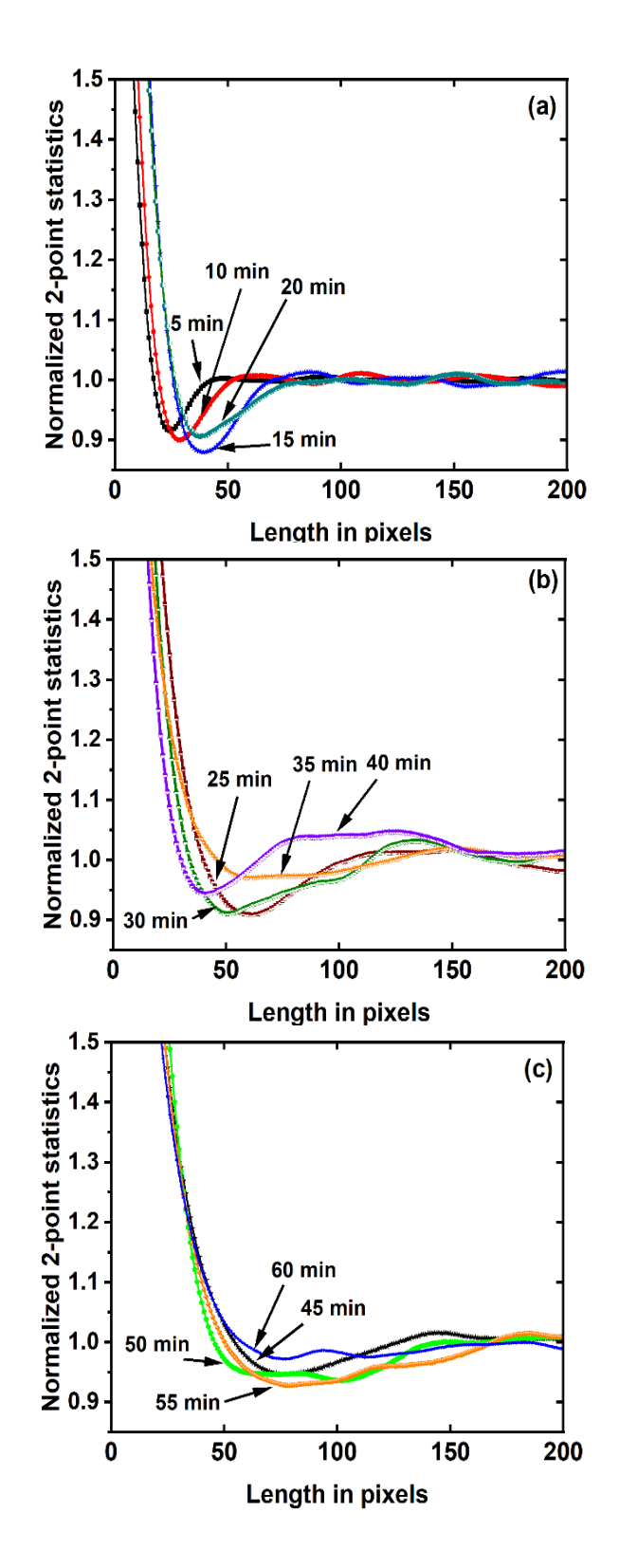


Figure 10. Normalized two-point statistics for (a) 5 to 20, (b) 25 to 40, and (c) 45 to 60 min films to an asymptotic value of around 1.

Figure 11a shows a plot of  $L_{\infty}$  versus sputtering time (that also can be considered as an average pore diameter) for the 5 – 60 min films. It reveals that, in general, the length of r increases with sputtering time. However, it has more variation in the 25 – 45 min films. The higher probability for the larger r with sputtering time indicates that the pore size has an increasing trend in which two sides of the r fall in the pore space. The values of  $L_{\infty}$  show that average pore size increases around three times in 60 min. The observation here is in agreement with what has been described before for the thick film. That is, the pore diameter increases with deposition time due to the shadowing effect in oblique-angle deposition. Another metric that can be extracted from the two-point statistics is the distance between the asymptotic value and the minimum value of the  $f_2^*$ , or d value, as shown in Figure 11b. The d value decreases with increasing sputtering time/film thickness. This metric shows an order of magnitude difference between 5 and 60 min films, and is also potentially related to morphological changes, such as clustering of pores.[35] Although both metrics change markedly with pore evolution as sputtering time increases, the d metric is more sensitive to the sputtering time, and may therefore be a valuable metric in capturing film evolution.

If the 2D peak of the original two-point function,  $f_2(\vec{r})$  is considered (as opposed to the non-directional statistics that are averaged over all directions), the shape of the peak provides an indication of local pore shape. Generally, for these films, the peak is elliptical in shape (see Figure 12). The maximum diameter of the two-point peak in Figure 11c shows an increasing trend in the diameter of the two-point peaks that reaches a plateau after 45 minutes. This reveals that by increasing the sputtering time, not only does pore extension increase, but the local pore diameter also increases (as might be expected). However, its value for the last four films remains constant, indicating that the channel diameter of the pores may have reached a limit, while the average pore area continues to grow; the resultant diffusion properties of the film for the higher sputtering times might be more controlled by the long-range connectivity rather than the short range connections.

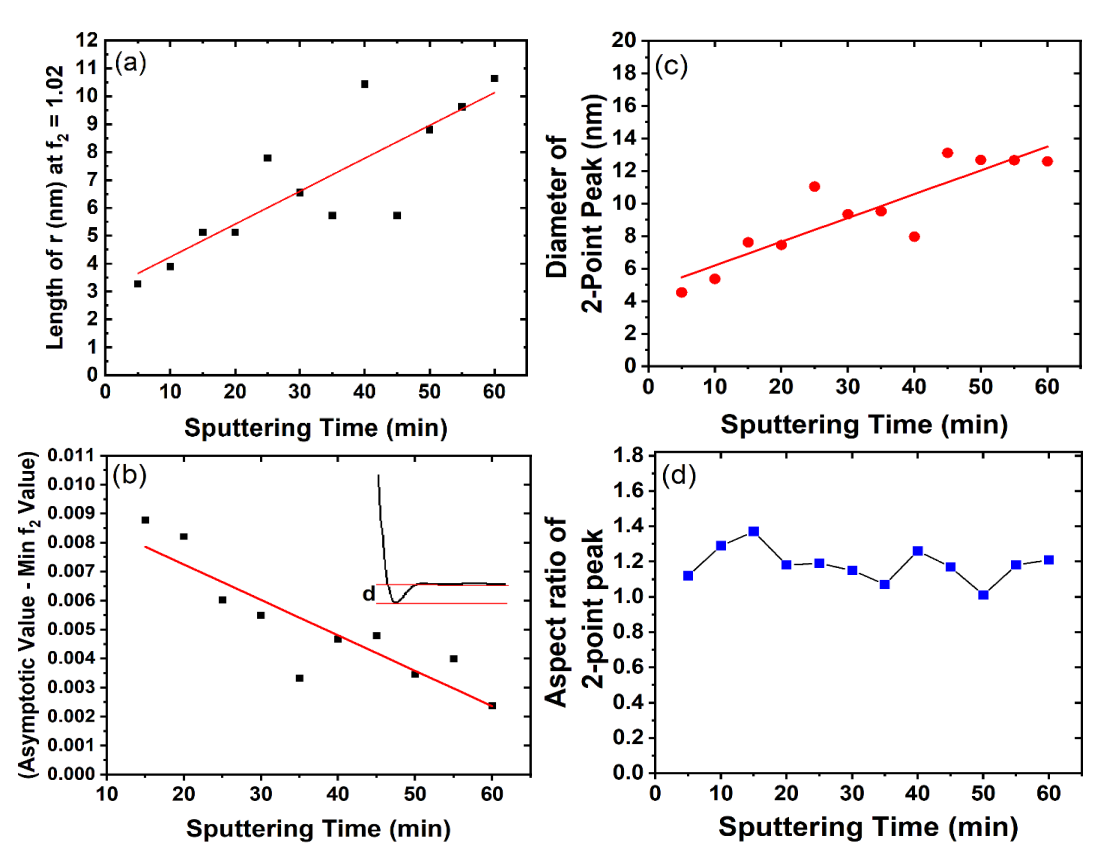


Figure 11. Plots of (a)  $L_{\infty}$  versus sputtering time; (b) the distance, d, between the asymptotic value and the minimum value of  $f_2^*$ ; (c) diameter and (d) aspect ratio of the two-point peak for the 5-60 min a-Si films.

Finally, the aspect ratio of the two-point peak, which can be interpreted as the local pore anisotropy, increases slightly for the first 15 min of sputtering (consistent with trends with other metrics, e.g., the moment of inertia in Figure 6), and then plateaus at around 1.2. Comparing the long-range connectivity expressed by the ratio of principal moment of inertia and the aspect ratio of the two-point peak in Figure 11d, both local and global anisotropy values show the same trend that agrees with the film growth model in oblique-angle sputtering.

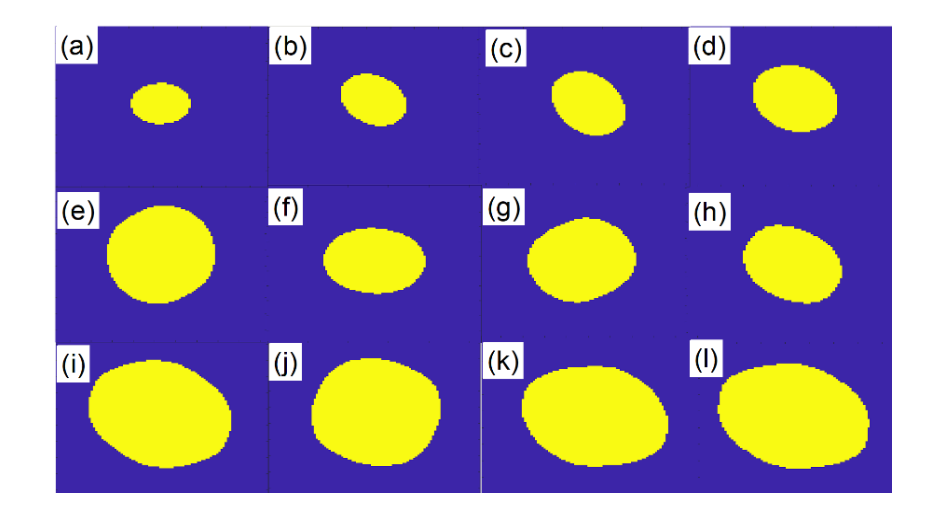


Figure 12. Local pore geometry based on the central two-point peak of the 5-60 min films in depositions times of (a) 5, (b) 10, (c) 15, (d) 20, (e) 25, (f) 30, (g) 35, (h) 40, (i) 45, (j) 50, (k) 55, and (l) 60 min.

## 3.2.2 Analyzing cross-section of a thick a-Si film to analyze of film growth in the z-direction

### 3.2.2.1 Contrast enhancement of a thick a-Si film via ZnO infiltration

Pore infiltration using a heavy element could be an ideal solution for increasing the contrast of a-Si micro/mesoporous films, and atomic layer deposition (ALD) may be a good candidate for this infiltration. Here, we infiltrated the porous a-Si films with ZnO by ALD. Zinc creates a high-contrast image when juxtaposed with silicon [30]. Average, horizontal EDS profiles of Zn, Si, and O obtained at the top, middle, and bottom of the infiltrated film (see Figure 13) showed similar levels of these elements, which suggests effective and quite uniform infiltration/penetration of ZnO throughout the entire film. A vertical (in the direction of film growth) EDS line scan (see Figure 14a) showed anticorrelated Si and Zn signals across multiple tilted, porous structures/pillars.

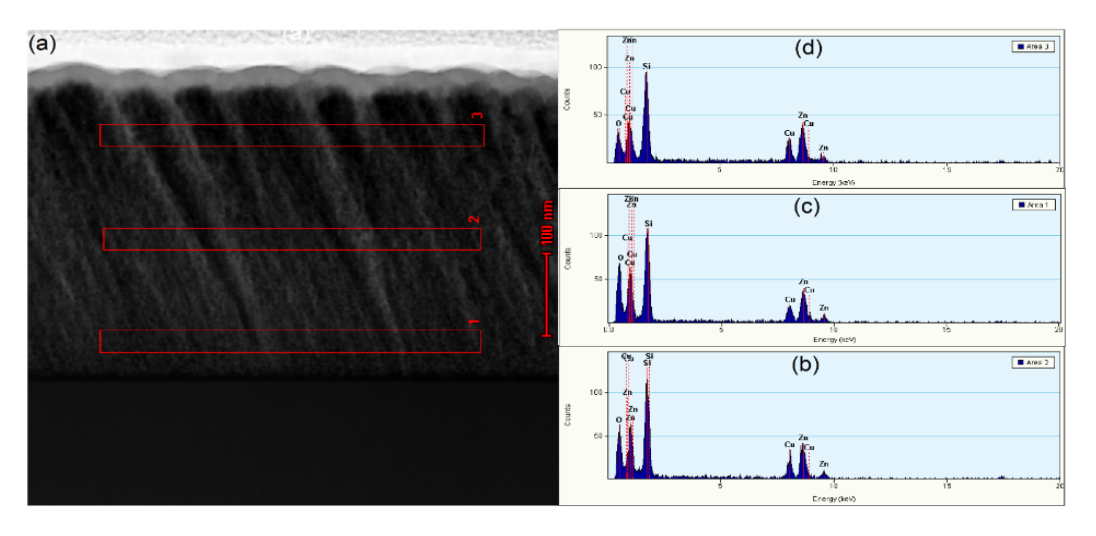


Figure 13. (a) Locations of average EDS scans across a STEM image of a cross-section of a ZnO infiltrated thick film of a-Si. Average, horizontal EDS scans at the (b) bottom, (c) middle, and (d) top of the film.

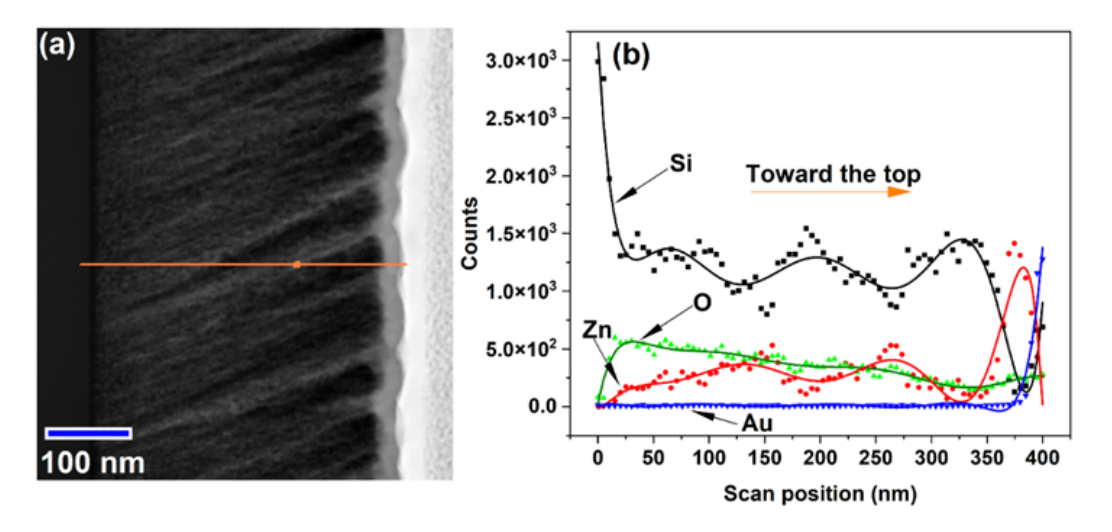


Figure 14. (a) Location of an EDS line scan in a STEM image and (b) EDS line scan profiles of Zn, Si, and O in a ZnO infiltrated a-Si film. Lines are guides to the eye.

Figure 15 shows STEM cross-sections of different regions of the ZnO-infiltrated sputtered a-Si film in Figure 14. The brighter areas correspond to ZnO deposited into the pores. This figure and Figure 14 show the type of tilted, hillock-like silicon structures that are commonly observed in oblique angle depositions [21]. A recent model presented by Gruner et al.,[21] showed that OAPVD growth of pillar structures takes place in three stages, which they named "initial", "transition", and "competition". In the initial stage, a fan structure grows in the direction of the

flux on the seeded layer. The transition stage occurs when shadowing effects begin, and the competition stage takes place when both sides of the pillars grow parallel to each other, reversing the shadowing effect. Similar growth can be observed in Figure 15a occurring at three tilt angles: 15° (from 0 to 100 nm), 11° (100 to 170 nm), and 22° (above 170 nm). These three growth regions are only apparent in the high contrast images of the ZnO-infiltrated structures.

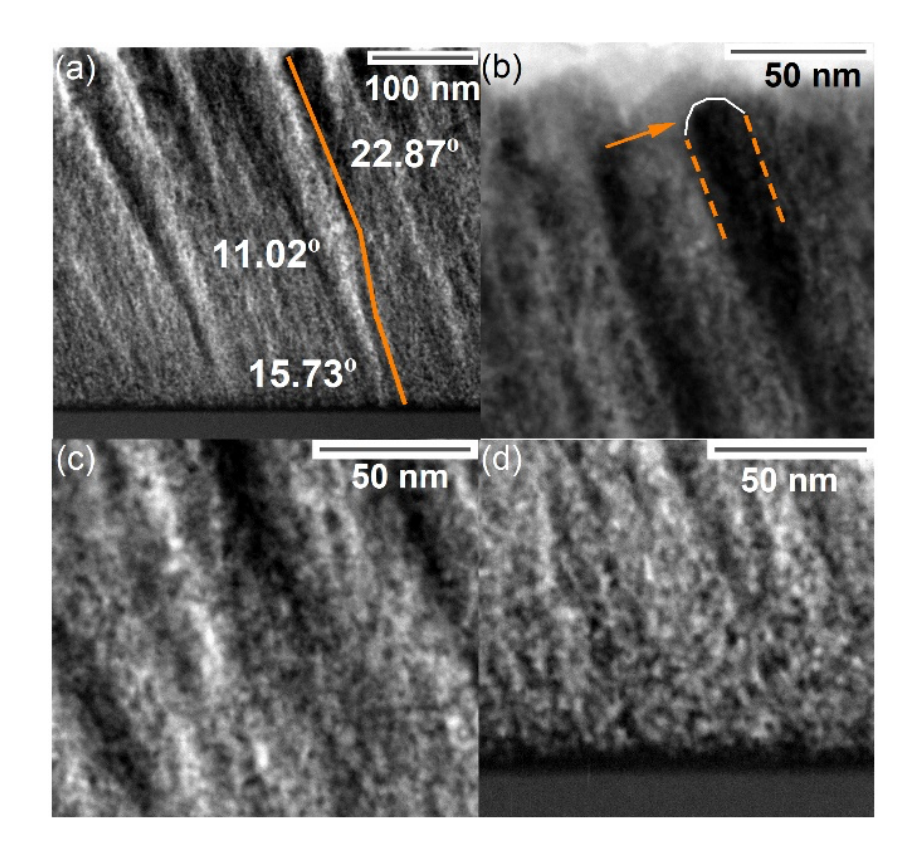


Figure 15. STEM cross-sectional images of (a) the entire ZnO-infiltrated a-Si film, and the (b) top, (c) middle, and (d) bottom of this film.

## 3.2.2.2 Quantitative morphological analysis of a ZnO-infiltrated cross-section of a thick a-Si film

Analyzing the cross-section of the thick, ZnO-infiltrated film (see Figure 16) can provide critical insights into its microstructure and properties at long deposition times. Figure 16 shows processed STEM images of different sections of this film including the entire film and regions at

its top, middle, and bottom. The results of applying the metrics developed above on these images are shown in Table 1; it is apparent that the average pore size increases from the bottom to the top of the film, consistent with the analysis given above on the thin samples. This implies that diffusion through the film is likely to be easiest in the z-direction.

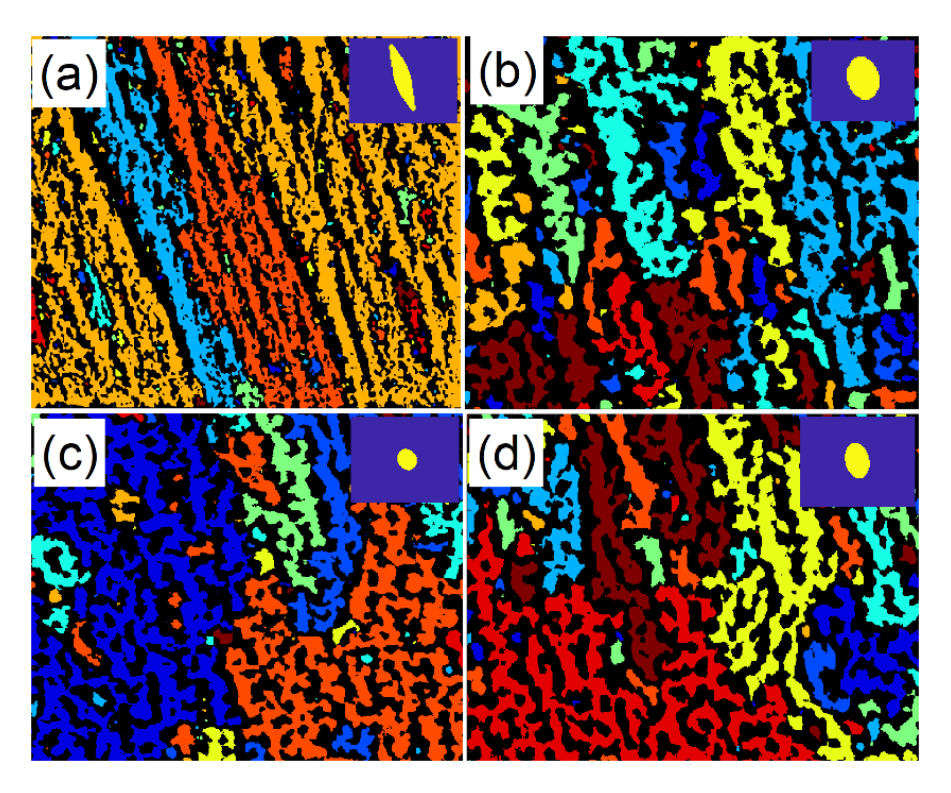


Figure 16. Random pore colored image of (a) the entire ZnO-infiltrated a-Si film, and the (b) top, (c) middle, and (d) bottom of this film; The related central two-point peak is attached on the top right corner of each image.

The relative surface areas (RSAs) of the middle and bottom of the thick ZnO-infiltrated film are approximately constant (see Table 1). However, the RSA is smaller at the top of the film. As noted for the 5-60 min films above, constant values of RSA for different sections of the film with increasing average pore area indicate uniform pore growth, i.e., the shape remains approximately constant despite the larger pore size. The low RSA value towards the top of the film indicates a higher surface area to volume ratio, arising from a more intricate boundary for the pores. As shown in Table 1, the average pore diameter for the three sections of the film are approximately the same and less than the average pore diameter of the whole film (again, due to high pore

connectivity in the z-direction). The average ratios of the principal moments of inertia are very high and show a very clear anisotropy toward the film's surface. Significant anisotropy in the z-direction might make the analyte's diffusion through the depth of the film easier. The Betti numbers, however, show almost the same trend as the 5 – 60 min films, as they have much lower values compared to the x-y cross sections studied above. Again, this shows that pore connectivity in the z-direction is much higher than in the x-y direction. The aspect ratio of the two-point peak is about the same for the top and bottom of the film, but lower values are observed in the middle. This reflects the fact that local pore geometry is more interrupted by the solid phase in the middle of the sample, i.e., there is significant morphological evolution during different growth stages. Finally, the porosity for the entire film and the cropped area are approximately the same at around 50%. This value is a little higher than the porosity in the x-y direction. We note that while some PVD films have much lower porosity (e.g. for anticorrosion films), our measured porosity values are in line with other studies using oblique angle sputtered films [23].

Table 1. Results of the characterization metrics on the ZnO-infiltrated cross-section of the thick a-Si film in Figure 16.

Property	Entire Film	Top	Middle	Bottom
Average pore area (nm <sup>2</sup> )	212	153	117	86
Relative surface area (RSA)	0.03	0.003	0.06	0.05
Average pore diameter (nm)	10.4	3.5	3.2	3
Average ratio of principal moments of inertia	119,200,000	1,395,000	600	14,150
Betti_0 number	268	65	98	93
Betti_1 number	551	853	452	211
Number of pores (larger than 0.58 nm <sup>2</sup> )	330	63	90	86
Aspect ratio of two-point peak	68	64	14	74
Porosity (%)	50	54	51	51

### **4 Conclusions**

To examine the morphology and evolution of the micro/mesoporous coatings used as support materials in SPME, various metrics, such as two-point autocorrelation functions, are employed. These metrics provide valuable insights into the properties of the coatings and can track

the growth of the films' morphology. In this study, a range of traditional and two-point based statistical metrics were used on high-resolution STEM images of oblique sputtered porous films. The quality and contrast of the STEM images were enhanced via ZnO infiltration. The analysis focused on a-Si thin films with different thicknesses, which were used to evaluate the evolution of the pore structure. Various approaches to quantify pore internal connectivity, pore geometry, and pore anisotropy were compared, with a particular emphasis on metrics that capture diffusion-related properties such as RSA that relates to the tortuosity, or complexity/length of the diffusion path.

- Porosity is the most typical volume fraction metric for analyzing voids, but contains no information about connectivity, anisotropy, or tortuosity, which are vital to the diffusion mechanism. The overall porosity was found to decrease slightly with sputtering time. Average size of connected pores grew steadily with sputtering time.
- Two-point statistics do not contain long-range connectivity information, but metrics based upon the non-directional two-point statistics have been used to indicate clustering behavior, for example. These metrics revealed a consistent trend in terms of evolution with sputtering time, that are indicators of local geometry changes. The characteristics of the local peak of the two-point autocorrelation function indicate the local pore shape, revealing an elliptical local pore geometry, with a small amount of anisotropy.
- Homology metrics contain information about the internal connectivity of pores, such as the number of connected pores (Betti\_0) and the number of loops or inclusions within pores (Betti\_1). These demonstrated a higher connectivity in pores as the sputtering time increased. Furthermore, Betti\_1 revealed an exponential decay in the number of a-Si islands within the pore space with longer sputtering time.

- Metrics based on principal moments of inertia indicate the extent of long range connectivity between pores and anisotropy of the connected pores, and also relate to ease of diffusion. The ratio of the first two principal moments of inertia was high, indicating high alignment of the pores in the growth direction. This ratio grew for the first 15 minutes of sputtering time, and then decreased to the original value, and remained stable after that.
- The relative surface area (RSA) metric quantifies the intricacy of the boundary between the pores and solid phases, or the branched nature of connected pores. For the architecture of the a-Si films, this relates to the tortuosity, or complexity/length of the diffusion path. This value rose only slightly with sputtering time, indicating that, while the pore size grew with sputtering time, the relative dimensions of the pores remained relatively constant.

In summary, this study showed that the average ratio of principal moment of inertia, Betti numbers, and two-point statistics-based metrics can capture information relating to morphology/ease-of-diffusion evolution during film growth. The metrics described herein are applicable to any porous material, irrespective of the preparation or imaging methods employed. The development and demonstration of these metrics is the first step towards more detailed processing-structure-property relations in these films; future work will include experimental and simulation based assessment of such relationships.

### Acknowledgment

This work was supported by Restek Corporation, USA. D. Fullwood was partially supported by NSF grant CMMI 2147126. We would like to acknowledge the BYU Electron Microscopy Facility for providing access to the equipment and expertise that allowed this project to be performed. We also thank Michael Standing, and Felipe Rivera (BYU Microscopy) for their help with the microscopy.

#### References

- [1] H.L. Lord, X. Zhang, F.M. Musteata, D. Vuckovic, J. Pawliszyn, In vivo solid-phase microextraction for monitoring intravenous concentrations of drugs and metabolites, Nat. Protoc. 6 (2011) 896–924. https://doi.org/10.1038/nprot.2011.329.
- [2] S. Azzi-Achkouty, N. Estephan, N. Ouaini, D.N. Rutledge, Headspace solid-phase microextraction for wine volatile analysis, Crit. Rev. Food Sci. Nutr. 57 (2017) 2009–2020.
- [3] J. Xu, G. Chen, S. Huang, J. Qiu, R. Jiang, F. Zhu, G. Ouyang, Application of in vivo solid-phase microextraction in environmental analysis, TrAC Trends Anal. Chem. 85 (2016) 26–35.
- [4] H. Piri-Moghadam, F. Ahmadi, J. Pawliszyn, A critical review of solid phase microextraction for analysis of water samples, TrAC Trends Anal. Chem. 85 (2016) 133–143.
- [5] M. Yu, A. Roszkowska, J. Pawliszyn, In Vivo Solid-Phase Microextraction and Applications in Environmental Sciences, ACS Environ. Au. 2 (2022) 30–41. https://doi.org/10.1021/acsenvironau.1c00024.
- [6] Q.-H. Zhang, L.-D. Zhou, H. Chen, C.-Z. Wang, Z.-N. Xia, C.-S. Yuan, Solid-phase microextraction technology for in vitro and in vivo metabolite analysis, TrAC Trends Anal. Chem. 80 (2016) 57–65.
- [7] B. Bojko, Solid-phase microextraction: a fit-for-purpose technique in biomedical analysis, Anal. Bioanal. Chem. 414 (2022) 7005–7013. https://doi.org/10.1007/s00216-022-04138-9.
- [8] J. Pawliszyn, 2 Theory of Solid-Phase Microextraction, in: J.B.T.-H. of S.P.M. Pawliszyn (Ed.), Elsevier, Oxford, 2012: pp. 13–59. https://doi.org/https://doi.org/10.1016/B978-0-12-416017-0.00002-4.
- [9] Y. Nolvachai, M.S.S. Amaral, R. Herron, P.J. Marriott, Solid phase microextraction for quantitative analysis Expectations beyond design?, Green Anal. Chem. 4 (2023) 100048. https://doi.org/https://doi.org/10.1016/j.greeac.2022.100048.
- [10] J. Ai, Solid Phase Microextraction for Quantitative Analysis in Nonequilibrium Situations, Anal. Chem. 69 (1997) 1230–1236. https://doi.org/10.1021/ac9609541.
- [11] N. Reyes-Garcés, E. Gionfriddo, G.A. Gómez-Ríos, M.N. Alam, E. Boyacı, B. Bojko, V. Singh, J. Grandy, J. Pawliszyn, Advances in Solid Phase Microextraction and Perspective on Future Directions, Anal. Chem. 90 (2018) 302–360. https://doi.org/10.1021/acs.analchem.7b04502.
- [12] H. Piri-Moghadam, M.N. Alam, J. Pawliszyn, Review of geometries and coating materials in solid phase microextraction: opportunities, limitations, and future perspectives, Anal. Chim. Acta. 984 (2017) 42–65.
- [13] A. Mehdinia, M. Fazlollah Mousavi, Enhancing extraction rate in solid-phase microextraction by using nano-structured polyaniline coating, J. Sep. Sci. 31 (2008) 3565–3572. https://doi.org/https://doi.org/10.1002/jssc.200800284.
- [14] A.C. Forse, K.A. Colwell, M.I. Gonzalez, S. Benders, R.M. Torres-Gavosto, B. Blümich,

- J.A. Reimer, J.R. Long, Influence of Pore Size on Carbon Dioxide Diffusion in Two Isoreticular Metal–Organic Frameworks, Chem. Mater. 32 (2020) 3570–3576. https://doi.org/10.1021/acs.chemmater.0c00745.
- [15] S. Torquato, M. Avellaneda, Diffusion and reaction in heterogeneous media: Pore size distribution, relaxation times, and mean survival time, J. Chem. Phys. 95 (1991) 6477–6489. https://doi.org/10.1063/1.461519.
- [16] C. Schlumberger, M. Thommes, Characterization of Hierarchically Ordered Porous Materials by Physisorption and Mercury Porosimetry—A Tutorial Review, Adv. Mater. Interfaces. 8 (2021) 2002181. https://doi.org/https://doi.org/10.1002/admi.202002181.
- [17] J. Kärger, D. Freude, Mass Transfer in Micro- and Mesoporous Materials, Chem. Eng. Technol. 25 (2002) 769–778. https://doi.org/https://doi.org/10.1002/1521-4125(20020806)25:8<769::AID-CEAT769>3.0.CO;2-0.
- [18] W. Wang, A. Svidrytski, D. Wang, A. Villa, H. Hahn, U. Tallarek, C. Kübel, Quantifying Morphology and Diffusion Properties of Mesoporous Carbon From High-Fidelity 3D Reconstructions, Microsc. Microanal. 25 (2019) 891–902. https://doi.org/10.1017/S1431927619014600.
- [19] D.M. Ruthven, J. Kärger, D.N. Theodorou, Diffusion in nanoporous materials, John Wiley & Sons, 2012.
- [20] J. Kaerger, Transport phenomena in nanoporous materials, ChemPhysChem. 16 (2015) 24–51.
- [21] C. Grüner, S. Liedtke, J. Bauer, S.G. Mayr, B. Rauschenbach, Morphology of Thin Films Formed by Oblique Physical Vapor Deposition, ACS Appl. Nano Mater. 1 (2018) 1370–1376. https://doi.org/10.1021/acsanm.8b00124.
- [22] V. Godinho, P. Moskovkin, R. Álvarez, J. Caballero-Hernández, R. Schierholz, B. Bera, J. Demarche, A. Palmero, A. Fernández, S. Lucas, On the formation of the porous structure in nanostructured a-Si coatings deposited by dc magnetron sputtering at oblique angles, Nanotechnology. 25 (2014) 355705. https://doi.org/10.1088/0957-4484/25/35/355705.
- [23] A. Barranco, A. Borras, A.R. Gonzalez-Elipe, A. Palmero, Perspectives on oblique angle deposition of thin films: From fundamentals to devices, Prog. Mater. Sci. 76 (2016) 59–153. https://doi.org/https://doi.org/10.1016/j.pmatsci.2015.06.003.
- [24] S. Torquato, H.W. Haslach Jr, Random heterogeneous materials: microstructure and macroscopic properties, Appl. Mech. Rev. 55 (2002) B62–B63.
- [25] R. Bostanabad, Y. Zhang, X. Li, T. Kearney, L.C. Brinson, D.W. Apley, W.K. Liu, W. Chen, Computational microstructure characterization and reconstruction: Review of the state-of-the-art techniques, Prog. Mater. Sci. 95 (2018) 1–41. https://doi.org/https://doi.org/10.1016/j.pmatsci.2018.01.005.
- [26] D.T. Fullwood, S.R. Niezgoda, B.L. Adams, S.R. Kalidindi, Microstructure sensitive design for performance optimization, Prog. Mater. Sci. 55 (2010) 477–562. https://doi.org/https://doi.org/10.1016/j.pmatsci.2009.08.002.
- [27] J. Fu, H.R. Thomas, C. Li, Tortuosity of porous media: Image analysis and physical simulation, Earth-Science Rev. 212 (2021) 103439. https://doi.org/https://doi.org/10.1016/j.earscirev.2020.103439.
- [28] A. Diwan, B. Singh, T. Roychowdhury, D. Yan, L. Tedone, P.N. Nesterenko, B. Paull, E.T. Sevy, R.A. Shellie, M. Kaykhaii, M.R. Linford, Porous, High Capacity Coatings for

- Solid Phase Microextraction by Sputtering, Anal. Chem. 88 (2016) 1593–1600. https://doi.org/10.1021/acs.analchem.5b03181.
- [29] T. Roychowdhury, D.I. Patel, D. Shah, A. Diwan, M. Kaykhaii, J.S. Herrington, D.S. Bell, M.R. Linford, Sputtered silicon solid phase microextraction fibers with a polydimethylsiloxane stationary phase with negligible carry-over and phase bleed, J. Chromatogr. A. 1623 (2020) 461065. https://doi.org/https://doi.org/10.1016/j.chroma.2020.461065.
- [30] L.E. Ocola, V. Sampathkumar, N. Kasthuri, R.P. Winarski, Contrast enhancement of biological nanoporous materials with zinc oxide infiltration for electron and X-ray nanoscale microscopy, Sci. Rep. 7 (2017) 1–8.
- [31] Peter Giblin, Graphs, Surfaces and Homology, Cambridge University Press, New York, 2010.
- [32] D.D. Gerrard, D.T. Fullwood, D.M. Halverson, S.R. Niezgoda, Computational Homology, Connectedness, and Structure-Property Relations, Comput. Mater. Contin. 15 (2010) 129–152.
- [33] D. Ormrod Morley, P.S. Salmon, M. Wilson, Persistent homology in two-dimensional atomic networks, J. Chem. Phys. 154 (2021) 124109.
- [34] ChomP software package, (2017).
- [35] S.E. Wilding, D.T. Fullwood, Clustering Metrics for two-phase Composites, J Comput. Mater. 50 (2011) 2262–2272.
- [36] A. Tewari, A.B. Gokhale, J.E. Spowart, D.B. Miracle, Quantitative characterization of spatial clustering in three-dimensional microstructures using two-point correlation functions, Acta Mater. 52 (2004) 307–319.
- [37] S. Yamashita, J. Kikkawa, K. Yanagisawa, T. Nagai, K. Ishizuka, K. Kimoto, Atomic number dependence of Z contrast in scanning transmission electron microscopy, Sci. Rep. 8 (2018) 12325. https://doi.org/10.1038/s41598-018-30941-5.
- [38] I.I. Vlasov, S. Turner, G. Van Tendeloo, A.A. Shiryaev, Chapter 9 Recent Results on Characterization of Detonation Nanodiamonds, in: O.A. Shenderova, D.M.B.T.-U.D. (Second E. Gruen (Eds.), William Andrew Publishing, Oxford, 2012: pp. 291–326. https://doi.org/https://doi.org/10.1016/B978-1-4377-3465-2.00009-8.
- [39] B. Ghanbarian, A.G. Hunt, R.P. Ewing, M. Sahimi, Tortuosity in Porous Media: A Critical Review, Soil Sci. Soc. Am. J. 77 (2013) 1461–1477. https://doi.org/https://doi.org/10.2136/sssaj2012.0435.
- [40] F.L. Tye, Tortuosity, J. Power Sources. 9 (1983) 89–100. https://doi.org/https://doi.org/10.1016/0378-7753(83)80026-3.
- [41] M. Sahimi, G.R. Gavalas, T.T. Tsotsis, Statistical and continuum models of fluid-solid reactions in porous media, Chem. Eng. Sci. 45 (1990) 1443–1502. https://doi.org/https://doi.org/10.1016/0009-2509(90)80001-U.
- [42] S.R. Niezgoda, D.T. Fullwood, S.R. Kalidindi, Delineation of the space of 2-point correlations in a composite material system, Acta Mater. 56 (2008). https://doi.org/10.1016/j.actamat.2008.07.005.